

Low-momentum relativistic nucleon-nucleon potentials I: Nuclear matter

Chencan Wang,^{1,*} Sibo Wang,² Hui Tong,³ Jinniu Hu,⁴ and Jiangming Yao¹

¹*School of Physics and Astronomy, Sun Yat-Sen University, Zhuhai 519082, China*

²*Department of Physics, Chongqing University, Chongqing 401331, China*

³*Helmholtz-Institut für Strahlen- und Kernphysik and Bethe Center for Theoretical Physics, Universität Bonn, D-53115 Bonn, Germany*

⁴*School of Physics, Nankai University, Tianjin, 300071, China*

(Dated: December 7, 2023)

A series of relativistic one-boson-exchange potentials for two-nucleon system, denoted as OBEPA, is constructed with a momentum cutoff Λ ranging from ∞ to 2 fm^{-1} . These potentials are developed by simultaneous fitting to nucleon-nucleon (NN) scattering phase shifts, low-energy scattering length, effective range, and the binding energy of the deuteron. The momentum-space matrix elements of the low-momentum OBEPA ($\Lambda \leq 3 \text{ fm}^{-1}$) demonstrate consistency with the universal behaviors observed in other realistic NN potentials evolved by renormalization group methods. These OBEPAs are applied to calculate the equation of state of symmetric nuclear matter (SNM) within either the nonrelativistic (NR) Brueckner-Hartree-Fock (BHF) or relativistic Brueckner-Hartree-Fock (RBHF) frameworks. The results show that the saturation properties of SNM are reproduced qualitatively from the RBHF calculation, but not from the NR-BHF calculation. This study highlights the relativistic mechanism in explaining the saturation properties of nuclear matter. The remaining discrepancy in reproducing empirical saturation properties in the RBHF calculation using the OBEPAs signals the necessity of including three-nucleon correlations or genuine three-nucleon forces.

I. INTRODUCTION

The nucleon-nucleon (NN) potential serves as a crucial input for nuclear *ab initio* calculations. Originating from the 1960s, the meson-exchange model stands as an effective framework for deriving realistic NN potentials [1–3]. Within this model, the one-boson exchange potentials (OBEPs), namely the Bonn potential and the highly accurate charge-dependent Bonn (CD-Bonn) potential, were proposed and remain frequently utilized in present-day *ab initio* calculations [4, 5]. The preservation of Dirac spinors and covariant operators in Bonn potentials enables the applicability to relativistic *ab initio* approaches, such as the relativistic Brueckner-Hartree-Fock (RBHF) theory. However, the original CD-Bonn potential, utilizing the pseudoscalar (ps) type of pion-nucleon (πN) coupling, cannot be employed in RBHF calculations for nuclear matter due to the unphysically large self-energies induced by the ps πN vertex [6]. Yet, by substituting the ps πN coupling with a pseudovector (pv) type, the modified CD-Bonn potentials become viable for relativistic applications [7, 8].

Over the past two decades, substantial progress has been made in developing NN potentials rooted in chiral effective field theory (chEFT) and renormalization group (RG) methods [9–13]. Consequently, various non-relativistic (NR) NN potentials have been formulated at different resolution scales, characterized by specific momentum cutoffs Λ [13–15]. Additionally, three-nucleon force (3NF) with specified cutoff Λ_{3N} arises naturally, either at the next-next-to-leading ($N^2\text{LO}$) order in chEFT

or through RG evolution in the flow equation [16–18]. In NR *ab initio* calculations, the cutoff dependence of few-body observables directly reflects the residual many-body forces [19, 20]. Furthermore, variations in many-body observables concerning Λ/Λ_{3N} provide insights into estimating theoretical uncertainties [15, 21–23]. This encourages the development of OBEPs with different momentum cutoffs Λ . Employing these potentials in relativistic *ab initio* calculations of nuclear many-body systems, such as nuclear matter, enables the exploration of cutoff-dependent equation of state (EOS) from a relativistic perspective.

Nuclear matter stands as a research topic of great interest in nuclear physics since it helps us understand the bulk properties of finite nuclei and the evolution of astrophysical objects like neutron stars. In particular, the properties of nuclear matter around the saturation density $n_0 = 0.16 \text{ fm}^{-3}$ provide benchmarks to test the validity of underlying NN potentials and many-body methods [24–27]. In addition, the knowledge of the EOS of nuclear matter at supra-saturation densities is important to understand the formation and structure of neutron stars [28–31], as well as the particle production in the heavy-ion collision (HIC) [32–34]. Early attempts to attack the problem were based on nonperturbative approaches such as NR variational method or Brueckner theory with traditional NN potentials [35–39].

It has been observed that the saturation properties of symmetric nuclear matter (SNM), derived from various NN potentials, align within the “Coester band”, systematically differing from the empirical saturation region [40–43]. This led to the conclusion that relying solely on NN potentials fails to quantitatively replicate correct saturation properties. This highlighted the pivotal role of 3NF in understanding the saturation mechanism of

* wangchc5@mail.sysu.edu.cn

nuclear matter [42, 44]. In contrast, the RBHF framework using only Bonn potentials, without explicit inclusion of 3NF, nearly reproduced SNM's saturation properties [4, 6]. RBHF theory hinges on two primary features: the effective Dirac spinor of nucleons, where the lower components rely on the effective Dirac mass, introducing additional density dependence in relativistic kinetics and the G -matrix; and the Lorentz structure of the self-energy, notably the attractive scalar self-energy and the repulsive timelike vector self-energy [45–47]. The emergence of saturation properties in SNM results from the intricate balance between the linearly increasing vector self-energy and the gradually diminishing scalar self-energy [48]. Recent progressions in this field involve the successful application of RBHF theory, notably in fully self-consistent calculations for finite nuclei [49, 50], and nuclear matter calculations encompassing the complete Dirac space [51, 52].

It's noteworthy that the availability of realistic NN potentials suitable for RBHF calculations is severely limited, primarily confined to the three Bonn potentials developed more than thirty years ago [4]. Additionally, these potentials lack specification regarding resolution scales, and the uncertainty assessment within the relativistic many-body method remains unexplored. To revitalize research in relativistic nuclear *ab initio* calculations, our initial step involves constructing a series of OBEPs, explicitly incorporating momentum cutoffs Λ (referred to as OBEP Λ s). These OBEP Λ s will be employed within the RBHF framework to compute the EOS of nuclear matter.

This paper is organized as follows. In Sec. II, the theoretical framework for OBEP, the scattering equation, and the RBHF theory for nuclear matter will be briefly reviewed. In Sec. III A, the fitting protocol and the parameters of OBEP Λ s will be given, and the potential matrix elements and the calculated NN observables with OBEP Λ s will also be provided. In Sec. III B, we will present nuclear matter results from both NR-BHF and RBHF calculations with these OBEP Λ s, shedding light on the implications of relativity in the saturation mechanism of SNM. Finally the summary and perspectives will be given in Sec. IV.

II. THEORETICAL FRAMEWORKS

A. One-boson-exchange potential and NN observables

Analogous to the Bonn potentials [4], present OBEP Λ s are developed based on the exchange of π , η in pv coupling, σ , δ mesons in scalar (s) coupling, and ω , ρ mesons in vector (v) coupling. These nucleon-meson interaction

Lagrangians are

$$\mathcal{L}^{(pv)} = -\frac{f_{pv}}{m_{pv}}\bar{\psi}\gamma^5\gamma^\mu\psi\cdot\partial_\mu\phi^{(pv)}, \quad (1a)$$

$$\mathcal{L}^{(s)} = +g_s\bar{\psi}\psi\cdot\phi^{(s)}, \quad (1b)$$

$$\mathcal{L}^{(v)} = -g_v\bar{\psi}\gamma^\mu\psi\cdot\phi_\mu^{(v)} - \frac{f_v}{2M}\bar{\psi}\sigma^{\mu\nu}\psi\cdot\partial_\mu\phi_\nu^{(v)}. \quad (1c)$$

The NN potential in the center-of-mass (CM) frame is obtained from tree-level Feynman amplitude:

$$V(\mathbf{q}', \mathbf{q}) = -\sum_a^{\text{all mes.}} \bar{u}_1(\mathbf{q}')\Gamma_a^{(1)}u_1(\mathbf{q})\frac{\mathcal{F}_a(Q^2)}{Q^2 + m_a^2} \times \bar{u}_2(-\mathbf{q}')\Gamma_a^{(2)}u_2(-\mathbf{q}). \quad (2)$$

Here, the subscript a represents all the six mesons, \mathbf{q} and \mathbf{q}' representing the incoming and outgoing relative momenta, u_i ($i = 1, 2$) for nucleon spinor and $\Gamma_a^{(i)}$ for different meson-nucleon coupling vertices. The $\mathbf{Q} = \mathbf{q}' - \mathbf{q}$ is three-momentum transfer. The form factor $\mathcal{F}_a(Q^2) = \exp[-(Q^2 + m_a^2)/\Lambda_a^4]$ is used on the meson propagator to alter the behavior of local momentum transfer, in which a meson-dependent parameter Λ_a is introduced. This choice of form factor is tested to be more suitable in our fitting procedure, and different from $(\Lambda_a^2 - m_a^2)/(\Lambda^2 + Q^2)^2$ used in the Bonn potentials.

In addition, we introduce the following non-local regulator

$$V_\Lambda(\mathbf{q}', \mathbf{q}) = \mathcal{R}(q')V(\mathbf{q}', \mathbf{q})\mathcal{R}(q), \quad (3)$$

with

$$\mathcal{R}(q) = \exp[-(q^{2n}/\Lambda^{2n})]. \quad (4)$$

The regulators above strongly suppress the matrix elements with relative momenta larger than the cutoff Λ .

The T matrix for the NN scattering process is obtained by the Thompson equation [4]:

$$T(\mathbf{q}', \mathbf{q}; W_q) = V_\Lambda(\mathbf{q}', \mathbf{q}) + \int \frac{d^3p}{(2\pi)^3} \frac{M^2}{E_p^2} V_\Lambda(\mathbf{q}', \mathbf{p}) \times \frac{1}{W_q - W_p + i\epsilon} T(\mathbf{p}, \mathbf{q}; W_q), \quad (5)$$

where $E_p = \sqrt{\mathbf{p}^2 + M^2}$ is the nucleon on-shell energy. $W_q = 2E_q$ and $W_p = 2E_p$ are the initial and intermediate two-nucleon energy in CM frame respectively. The partial-wave scattering matrix is obtained by

$$\mathcal{S}_{\ell'\ell} = \delta_{\ell'\ell} - i\pi \frac{qM^2}{E_q} \langle \ell' s j | T(W_q) | \ell s j \rangle. \quad (6)$$

Corresponding phase shifts δ in uncoupled channel are given by $\mathcal{S}_{\ell\ell} = e^{i2\delta_\ell}$. For coupled channels, the phase shifts $\delta_{\ell\pm 1}$ and mixing angle ϵ_j are obtained by

$$\begin{pmatrix} \mathcal{S}_{--} & \mathcal{S}_{-+} \\ \mathcal{S}_{+-} & \mathcal{S}_{++} \end{pmatrix} = \begin{pmatrix} \cos 2\epsilon_j e^{2i\delta_-} & i \sin 2\epsilon_j e^{i(\delta_- + \delta_+)} \\ i \sin 2\epsilon_j e^{i(\delta_- + \delta_+)} & \cos 2\epsilon_j e^{2i\delta_+} \end{pmatrix}, \quad (7)$$

where \pm stand for $\ell = j \pm 1$.

The binding energy E_d and wave functions $(\psi_S, \psi_D)^T$ of deuteron are obtained by solving the following homogeneous Thompson equation

$$\begin{pmatrix} \psi_S(q) \\ \psi_D(q) \end{pmatrix} = \frac{1}{2M - E_d - W_q} \int_0^{+\infty} p^2 dp \frac{M^2}{E_p^2} \times \begin{pmatrix} V_{\Lambda,SS}(q,p) & V_{\Lambda,SD}(q,p) \\ V_{\Lambda,DS}(q,p) & V_{\Lambda,DD}(q,p) \end{pmatrix} \begin{pmatrix} \psi_S(p) \\ \psi_D(p) \end{pmatrix}. \quad (8)$$

B. The RBHF theory with projection method

The single-nucleon motion in nuclear matter follows the Dirac equation

$$[\boldsymbol{\alpha} \cdot \mathbf{k} + \beta M + \beta \Sigma(k)]u(\mathbf{k}, \lambda) = E_k u(\mathbf{k}, \lambda), \quad (9)$$

The self-energy in nuclear matter can be expressed as $\Sigma = \Sigma_S - \gamma^0 \Sigma_0 + \boldsymbol{\gamma} \cdot \mathbf{k} \Sigma_V$, where Σ_S , Σ_0 , and Σ_V represent the scalar self-energy, time-like and space-like vector self-energies, respectively. Here, $\lambda = \pm 1/2$ denotes helicity.

With the definitions of reduced Dirac mass and effective energy

$$M^* = \frac{M + \Sigma_S}{1 + \Sigma_V}, \quad E_k^* = \frac{E_k - \Sigma_0}{1 + \Sigma_V}, \quad (10)$$

the solutions to the Dirac equation are $E_k^* = \sqrt{\mathbf{k}^2 + M^{*2}}$ and plane-wave spinor

$$u(\mathbf{k}, \lambda) = \sqrt{\frac{E_k^* + M^*}{2M^*}} \begin{pmatrix} 1 \\ \frac{\boldsymbol{\sigma} \cdot \mathbf{k}}{M^* + E_k^*} \end{pmatrix} |\lambda\rangle. \quad (11)$$

The effective NN potential in nuclear matter is obtained with the Brueckner G -matrix:

$$\begin{aligned} G(\mathbf{q}', \mathbf{q}|\mathbf{P}, W_q) &= V_\Lambda(\mathbf{q}', \mathbf{q}) + \int \frac{d^3 p}{(2\pi)^3} \frac{M^{*2}}{E_p^{*2}} V_\Lambda(\mathbf{q}', \mathbf{p}) \\ &\times \frac{Q(\mathbf{p}, \mathbf{P})}{W_q - W_p + i\varepsilon} G(\mathbf{p}, \mathbf{q}|\mathbf{P}, W_q), \quad (12) \end{aligned}$$

where \mathbf{P} is the CM momentum and Q is Pauli blocking operator prohibiting nucleon scattering into occupied states.

As illustrated in Ref. [6], the scalar and time-component vector self-energies may exhibit unphysically large values due to the inadequate treatment of the one-pion-exchange potential V_π . To mitigate this issue, the subtracted T -matrix scheme is proposed, wherein the G -matrix is split into two components, $G = V_{\text{pv}} + \Delta G$, and $V_{\text{pv}} = V_\pi + V_\eta$. The transformation of ΔG from the $\ell s j$ representation to partial-wave helicity representation enables the derivation of invariant amplitudes F .

$$\Delta G = F_S \Gamma_S + F_V \Gamma_V + F_T \Gamma_T + F_P \Gamma_P + F_A \Gamma_A, \quad (13)$$

with the pseudoscalar-type covariant basis

$$\Gamma_S = \mathbf{1}_1 \otimes \mathbf{1}_2, \quad (14a)$$

$$\Gamma_V = (\gamma^\mu)_1 \otimes (\gamma_\mu)_2, \quad (14b)$$

$$\Gamma_T = (\sigma^{\mu\nu})_1 \otimes (\sigma_{\mu\nu})_2, \quad (14c)$$

$$\Gamma_A = (\gamma^5 \gamma^\mu)_1 \otimes (\gamma^5 \gamma_\mu)_2, \quad (14d)$$

$$\Gamma_P = (\gamma^5)_1 \otimes (\gamma^5)_2. \quad (14e)$$

The self-energies generated by ΔG can be calculated by

$$\Sigma_S(k) = \int \frac{d^3 k'}{(2\pi)^3} \frac{M^*}{E_{k'}^*} F_S(q, q), \quad (15a)$$

$$\Sigma_0(k) = - \int \frac{d^3 k'}{(2\pi)^3} F_V(q, q), \quad (15b)$$

$$\Sigma_V(k) = - \frac{1}{k^2} \int \frac{d^3 k'}{(2\pi)^3} \frac{\mathbf{k} \cdot \mathbf{k}'}{E_{k'}^*} F_V(q, q), \quad (15c)$$

where $q = \frac{1}{2}\sqrt{s^* - 4M^{*2}}$ is the relative momentum in two-nucleon CM frame, $s^* = (E_k^* + E_{k'}^*)^2 - (\mathbf{k} + \mathbf{k}')^2$.

The remaining V_{pv} is decomposed in complete pseudovector representation, corresponding formulae for self-energies are complicated, see Ref. [6] for details. Numerical computations demonstrate that the contributions from V_{pv} to self-energies are approximately one order of magnitude smaller than those originating from ΔG .

The Brueckner G -matrix (12) is solved by iteration. After convergence, the binding energy per-nucleon in nuclear matter is given by $E/A = E_{\text{kin}}/A + E_{\text{pot}}/A$, where the kinetic term is calculated by

$$E_{\text{kin}}/A = \frac{1}{n} \sum_\lambda \int^{k_F} \frac{d^3 k}{(2\pi)^3} \langle \bar{u}(\mathbf{k}, \lambda) | \boldsymbol{\gamma} \cdot \mathbf{k} + M | u(\mathbf{k}, \lambda) \rangle - M, \quad (16)$$

with n representing the nucleon number density. The average potential energy is given by

$$\begin{aligned} E_{\text{pot}}/A &= \frac{1}{n} \sum_\lambda \int^{k_F} \frac{d^3 k}{(2\pi)^3} \langle \bar{u}(\mathbf{k}, \lambda) | \\ &\times (M^* \Sigma_S / E_k^* - \Sigma_0 + k^2 \Sigma_V / E_k^*) | u(\mathbf{k}, \lambda) \rangle. \quad (17) \end{aligned}$$

III. RESULTS AND DISCUSSIONS

A. The fitting procedure and NN observables

The parameters in the OBEP in Eq. (2) are determined by minimizing the objective function

$$\begin{aligned} f(\mathbf{X}) &= \sum_\delta w_\delta^2 (\delta - \delta_{\text{NPWA}})^2 + w_d^2 (E_d - E_d^{(\text{expt})})^2 \\ &+ \sum_S \left[w_a^2 (a_S - a_S^{(\text{expt})})^2 + w_r^2 (r_S - r_S^{(\text{expt})})^2 \right], \quad (18) \end{aligned}$$

TABLE I. Mesons parameters in OBEPAs with the variation of cutoffs Λ (in unit fm^{-1}). In each row, the coupling parameters are given as g_a (Λ_a). The meson masses (in the parenthesis after each meson) and Λ_a are given in unit GeV. For pion and eta meson, we take $g_a = 2Mf_a/m_a$, where the mass of nucleon is the averaged value $M = 938.919$ MeV. ρ meson coupling constants are given in the form of $g_\rho - f_\rho/g_\rho$.

Λ	π (0.138)	ω (0.783)	ρ (0.770)	η (0.548)	δ (0.983)	σ (0.550)
∞	12.71 (0.97)	14.81 (1.05)	2.38–6.0 (0.90)	1.29 (0.77)	9.02 (0.96)	10.28 (1.83)
5	12.69 (0.97)	14.28 (1.03)	2.16–6.8 (0.97)	4.59 (0.77)	8.07 (0.95)	10.27 (1.75)
4	12.66 (0.93)	13.55 (1.00)	2.23–6.9 (1.01)	5.20 (0.77)	8.80 (0.87)	9.95 (1.50)
3	12.67 (0.91)	12.98 (0.97)	2.42–6.8 (1.03)	5.06 (0.77)	10.31 (0.81)	9.70 (1.32)
2	13.20 (0.90)	12.15 (0.94)	2.89–5.7 (1.04)	0.00 (0.77)	10.38 (0.78)	9.32 (1.23)

where \mathbf{X} contains 12 variables, including g_a (f_a) and Λ_a for the six mesons. The neutron-proton (np) phase shifts of partial wave $j \leq 4$ with laboratory energy $E_{\text{lab}} \leq 300$ MeV are calculated to compare with phase shifts from Nijmegen partial-wave analyse (NPWA) [53]. $E_d^{(\text{expt})} = 2.2246$ MeV is the binding energy of deuteron. The low-energy scattering observables [54], namely the S -wave scattering lengths $a_{1S_0}^{(\text{expt})} = -23.75$ fm, $a_{3S_1}^{(\text{expt})} = 5.42$ fm, and effective ranges $r_{1S_0}^{(\text{expt})} = 2.75$ fm, $r_{3S_1}^{(\text{expt})} = 1.76$ fm are also included in the fitting. w_δ, w_d, w_a, w_r are the weighting factors, we employ $w_\delta = 1/(\Delta\delta_{\text{NPWA}})$, with $\Delta\delta_{\text{NPWA}}$ being the phase shift uncertainty in NPWA. We employ $w_d = 1000$ and $w_r, w_a = 100$ to ensure both partial-wave phase shifts and low-energy observables can be simultaneously reproduced.

During the fitting, $n = 3$ is applied in the regulator (3) for $\Lambda \geq 4 \text{ fm}^{-1}$, and $n = 4$ is used for $\Lambda \leq 3 \text{ fm}^{-1}$. Slightly different parameterizations for the six mesons are allowed to minimize $f(\mathbf{X})$ at each cutoff, but the nuclear matter results are insensitive to such small changes in parameters. The mesons' parameters are finally determined at each Λ by both minimizing $f(\mathbf{X})$ and considering the continuity between adjacent cutoffs. These parameters are listed in Tab. I. In Fig. 1, variations of meson-nucleon coupling constants with respect to decreasing cutoffs are plotted. As shown in the figure, g_π, g_ρ , and f_ρ/g_ρ only vary a little, while g_σ and g_ω are monotonously decreasing with Λ . The g_η and g_δ show nonmonotonic behaviors, and the η meson finally turns out to be redundant at $\Lambda = 2 \text{ fm}^{-1}$ according to the minimization procedure. For comparison, meson-nucleon coupling constants from relativistic Hartree-Fock (RHF) density functional parameter sets, such as PKA1, PKO*i* ($i = 1, 2, 3$) [55, 56], are also plotted in the form of error bars, according to their statistical mean values and standard deviations. It can be found that present coupling constants from OBEPAs have the tendencies to close those of RHF model at low cutoff.

The phase shifts with $j \leq 2$, calculated using OBEPAs and depicted in Fig. 2, demonstrate good agreement with the NPWA analysis [53] up to $E_{\text{lab}} = 200$ MeV. This congruence extends to the peripheral partial waves in our calculations. However, for $E_{\text{lab}} > 200$ MeV, discernible deviations arise, particularly noticeable in the 1P_1 channel. Although this channel is specially treated

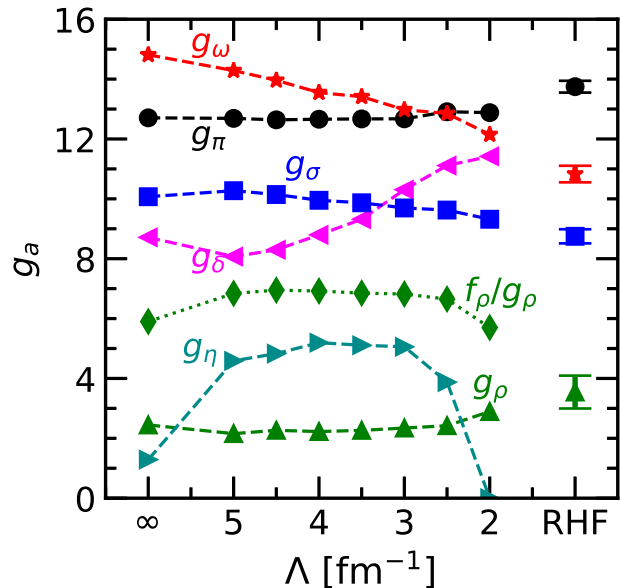


FIG. 1. The meson-nucleon coupling constants g_a running with external relative momentum cutoff Λ . The error bars are statistic mean values and standard deviations of meson-nucleon coupling parameters for the RHF approaches [55, 56].

in both Bonn potentials and the CD-Bonn potential, in our work, there are no specific partial-wave refinements in . Tab. II presents the deuteron properties computed using OBEPAs. Remarkably, properties such as the matter radius r_d , quadrupole moment Q_d , and asymptotic D/S ratio remain largely invariant despite variations in cutoffs, while the D -state probability P_D gradually diminishes as Λ decreases. P_D is related to the tensor components of NN interaction, when the cutoffs decreases, the tensor components are suppressed. This reduction in P_D reflects an understanding that it is not a directly observable; its dependence on the cutoff is also observed in the RG evolution as documented in [57].

Figure 3 displays a comparison of momentum-space matrix elements in the 1S_0 channels of OBEPAs ($\Lambda \leq 4 \text{ fm}^{-1}$) with other realistic NN potentials, including OBEP ∞ , the CD-Bonn potential [5], Argonne $v18$ (AV18) [58], and the chiral nuclear force at the fifth or-

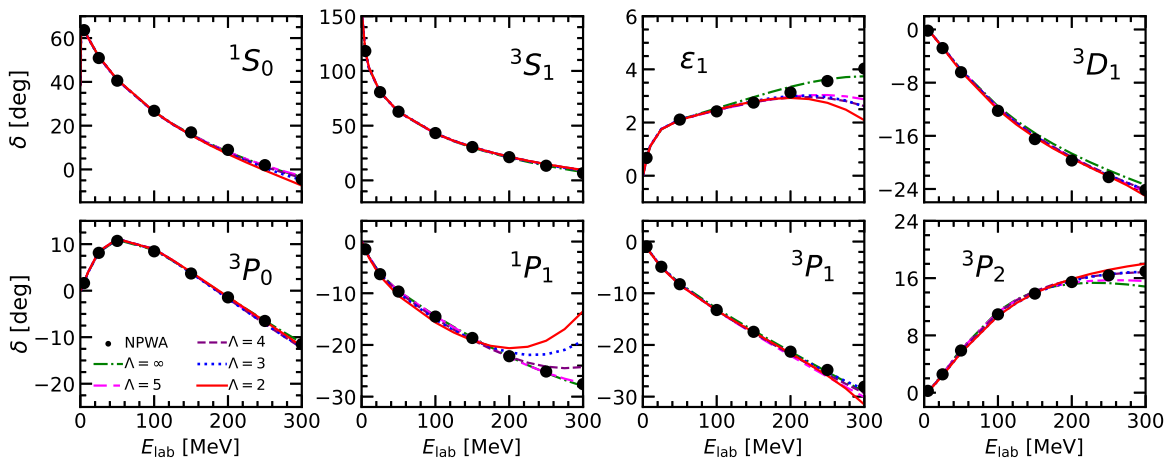


FIG. 2. Neutron-proton partial-wave phase shifts $j \leq 2$ calculated with the OBEPAs.

TABLE II. Deuteron properties predicted by OBEPAs. r_d is the matter radius, Q_d is the quadrupole momentum, D/S is the ratio of asymptotic D and S state amplitudes, and P_D is the D -state probability.

Λ	r_d [fm]	Q_d [fm^2]	D/S	P_D (%)
∞	1.967	0.2634	0.0247	5.498
5	1.967	0.2630	0.0246	5.429
4	1.964	0.2625	0.0246	5.205
3	1.964	0.2634	0.0246	4.827
2	1.967	0.2634	0.0248	4.246
expt.	1.975	0.2859	0.0256	

der (with the original cutoff $\Lambda_\chi = 500$ MeV, denoted as $N^4\text{LO}$) evolved by a smooth RG technique [57, 59]. In the left panels (a), (b), and (c), on-shell 1S_0 potential elements are provided. These panels reveal that as Λ decreases to $\Lambda \leq 3 \text{ fm}^{-1}$, the on-shell potential matrix elements of CD-Bonn, AV18, $N^4\text{LO}$, and our OBEPAs converge closely. The corresponding half-on-shell potential matrix elements in the right panels (a'), (b'), and (c') generally mirror the trends observed in the on-shell cases. Similar behavior is noted in potential matrix elements of other partial-wave channels. Notably, the potential matrix elements of OBEPAs closely resemble those of other realistic potentials after RG evolution down to $\Lambda = 2 \text{ fm}^{-1}$, clearly demonstrating the universality of phase-shift equivalent NN potentials [12].

B. Nuclear matter results

The OBEPAs potentials are utilized in nuclear matter calculations employing both NR-BHF and RBHF approaches. The resulting EOSs are depicted in Fig. 4, with the saturation points of each curve indicated. In the NR calculations, OBEPAs are augmented with minimal rel-

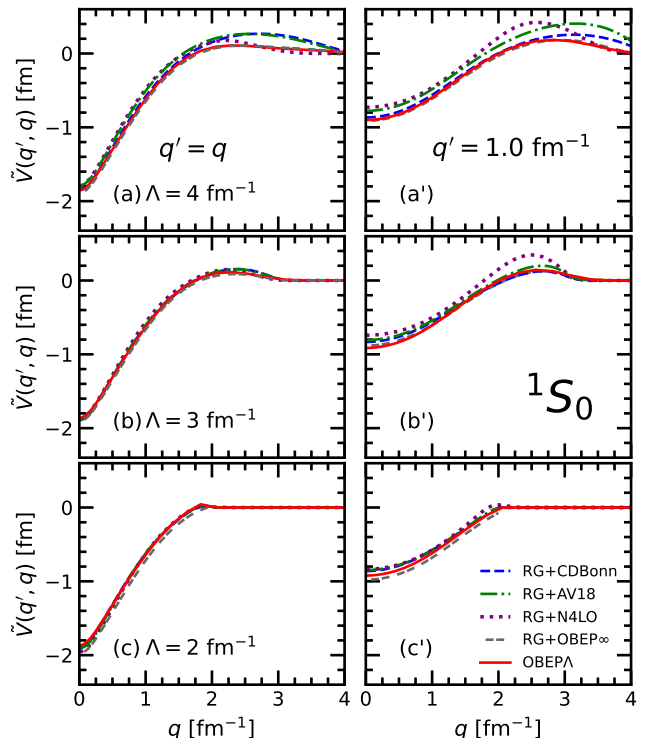


FIG. 3. The matrix elements of on-shell (left panels) and half-on-shell (right panels) OBEPAs potentials in the 1S_0 channel, in comparison with other RG evolved realistic NN potentials, including CD-Bonn, AV18 and $N^4\text{LO}$. Here we use the same convention as Ref. [12], $\tilde{V}(q', q) = \pi M V(q', q)/2$.

ativity [60],

$$V_{\Lambda, \text{NR}}(\mathbf{q}', \mathbf{q}) = \sqrt{\frac{M}{E_{q'}}} V_{\Lambda}(\mathbf{q}', \mathbf{q}) \sqrt{\frac{M}{E_q}}, \quad (19)$$

while BHF calculations are executed under the continuous choice method [61].

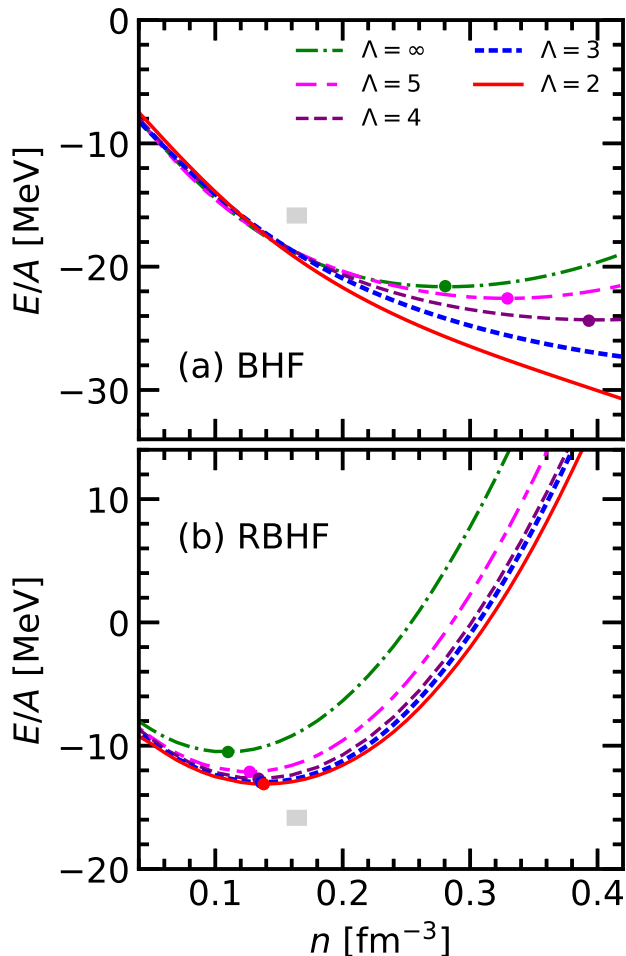


FIG. 4. The energy per nucleon for the symmetric nuclear matter calculated by BHF and RBHF approaches with different OBEPs. The shaded area indicates the empirical saturation region with density $n = 0.164 \pm 0.007 \text{ fm}^{-3}$ and $E/A = -15.86 \pm 0.57 \text{ MeV}$ [23]. The energy minimum of each curve is marked by a dot.

In panel (a) of Fig.4, the NR-BHF results exhibit convergence before reaching the empirical saturation region, although they notably display an overbound nature. These findings qualitatively align with the outcomes from Refs. [15, 57], particularly in instances where, at low cutoffs, the bare potentials demonstrate quantitative proximity, as depicted in Fig.3. However, as densities surpass the empirical saturation region, the divergence of NR EOSs becomes evident. The extent of overbinding corresponds to the chosen cutoffs; notably, for cutoffs lower than 3 fm^{-1} , no saturation points are observed in the region $n \leq 4 \text{ fm}^{-3}$. This absence underscores the necessity of incorporating 3NFs to elucidate the saturation mechanism for softer NN potentials in NR frameworks.

In panel (b), the situation regarding relativistic results differs notably. All RBHF calculations conducted with OBEPs manifest saturation phenomena. How-

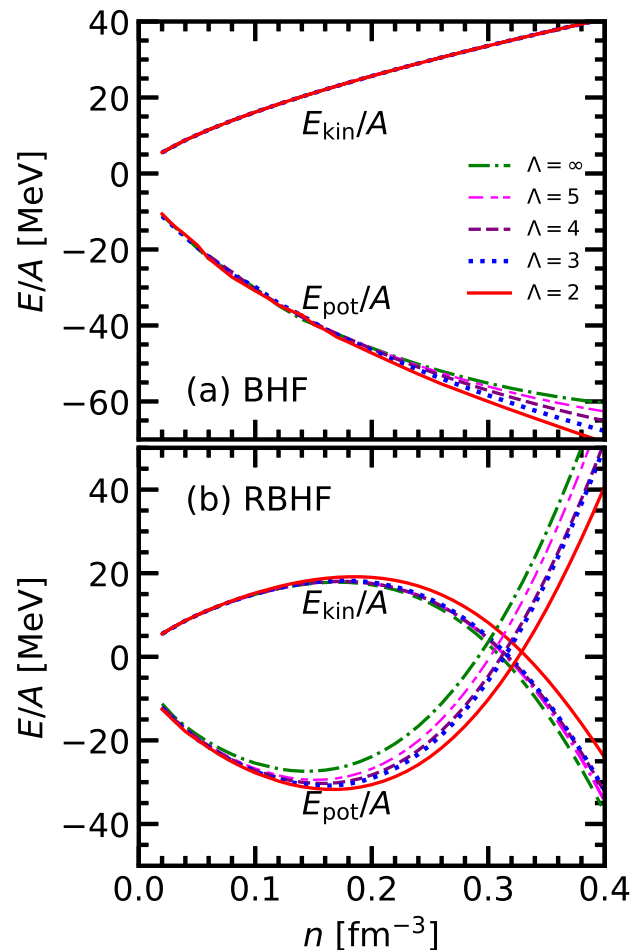


FIG. 5. The kinetic and potential terms obtained by BHF calculation in panel (a) and RBHF calculation in panel (b), with OBEPs as input.

ever, the binding energy and density at each saturation point do not align adequately with those observed in the empirical saturation region, even with the softest potential at $\Lambda = 2 \text{ fm}^{-1}$. The convergence patterns of resulting EOSs in relation to cutoff variation also diverge from their non-relativistic counterparts; notably, the gaps between adjacent cutoffs decrease as the cutoff decreases. The disparity between current RBHF calculations and empirical saturation properties might possibly be attributed to unaccounted relativistic 3NF, or the exclusion of higher-order contributions in Bethe-Brueckner-Goldstone (BBG) expansion, which warrants exploration in future studies. Additionally, it's important to note that while the original Bonn A potential can nearly reproduce saturation properties [4], but some of its phase shift predictions, especially the mixing parameter ϵ_1 in the 3S_1 - 3D_1 channel, deviate considerably from NPWA even at very small E_{lab} . In contrast, all the OBEPs successfully reproduce ϵ_1 up to $E_{\text{lab}} = 200 \text{ MeV}$.

To clarify the differences between BHF and RBHF re-

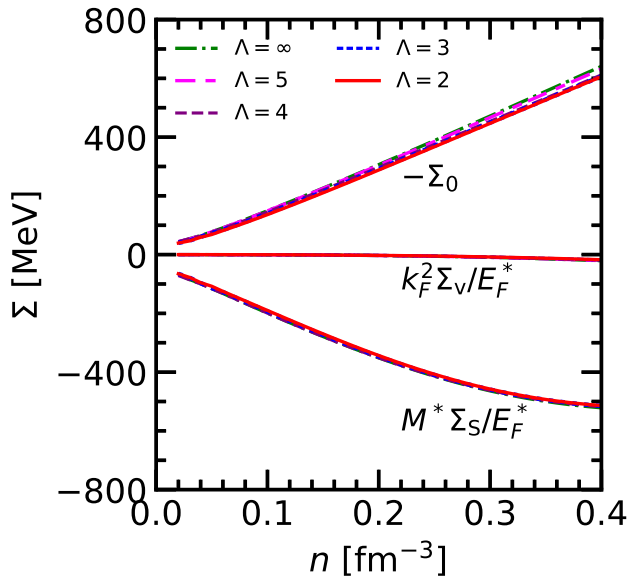


FIG. 6. The self-energy components at Fermi momentum k_F obtained in RBHF calculations with OBEPAs.

sults with the OBEPAs, we show in Fig. 5 the kinetic and potential terms obtained from BHF and RBHF calculations respectively. For BHF calculation in panel (a), the kinetic terms are all the same as free Fermi gas, while the potential terms vary with cutoffs, which are in correspondance with the divergence of EOSs shown in panel (a) of Fig. 4. For RBHF calculations in panel (b), as Eq. (16) indicates, the kinetic mass equals to the expectation value of relativistic kinetic operator $\gamma \cdot \mathbf{k} + M$ minus rest mass. Before empirical saturation density, the two kinetic contributions are close. Since Dirac mass appears in the lower component of spinor $u(\mathbf{k}, \lambda)$, the expectation value of relativistic kinetic operator can be even smaller than the rest nucleon mass at large densities.

The relativistic potential terms from Eq. (17), plotted in panel (b) of Fig. 5 gain considerable repulsion as compared with BHF results. To understand the source of repulsion in relativistic potential contributions, we present in Fig. 6 the self-energy components appearing in Eq. (17). Since Σ_V are one order of magnitude smaller than Σ_0 and Σ_S , we will mainly focus on Σ_0 and Σ_S . By relativistic decomposition of ΔG as Eq. (13) and V_{pv} in complete pv representation, both attractive Σ_S and repulsive $-\Sigma_0$ as large to several hundreds are generated for all cutoffs. The attractive Σ_S gets quenched at large densities, due to a factor M^*/E_k^* present in the integrand of Eq. (15a), while $-\Sigma_0$ increases almost linearly with increasing density. The cancellation between $M^*\Sigma_S/E_k^*$ and $-\Sigma_0$ finally leads to considerable repulsion in Eq. (17) compared to BHF calculations.

At zero temperature, the pressures of symmetric nuclear matter, given by $P = n^2 \frac{\partial(E/A)}{\partial n}$, are computed via both BHF and RBHF calculations utilizing OBEPAs as

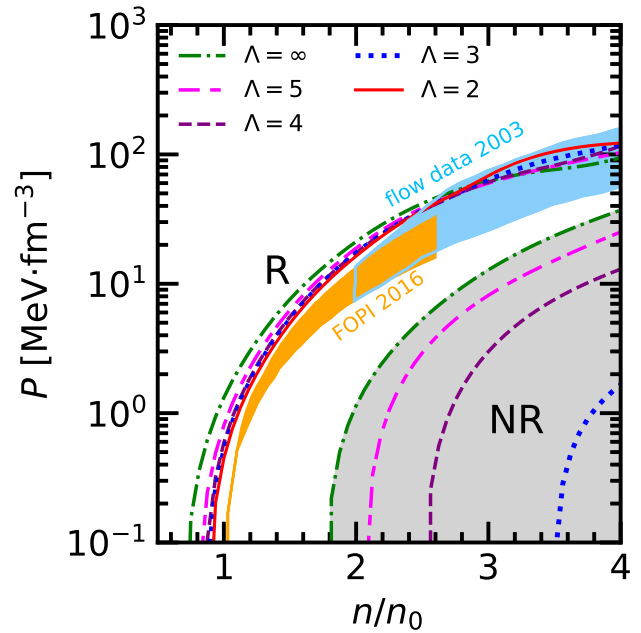


FIG. 7. The pressure of symmetric nuclear matter at zero temperature obtained by BHF and RBHF calculations with OBEPAs (to distinguish, the NR-BHF results are shaded in grey). The shaded areas in orange and cyan are experimental constraints from HIC experiments.

functions of density. Illustrated in Fig. 7, the shaded areas represent constraints established by HIC experiments, labeled as "flow data 2003" [32] and "FOPI 2016" [33]. BHF calculations yield EOSs that are too soft to satisfy the constraints imposed by HIC experiments. Conversely, RBHF calculations, attributed to significant relativistic repulsion, generate EOSs that better align with the experimental constraints. Moreover, the causality is automatically encoded in relativistic calculations, manifested in $c_s^2 = \frac{\partial P}{\partial \epsilon} < 1$, with ϵ being the energy density.

IV. SUMMARY AND OUTLOOK

We constructed one-boson-exchange potentials by introducing exponential regulators with relative momentum cutoffs ranging from $\Lambda = \infty$ to 2 fm^{-1} . The regulator effectively suppress high momenta beyond the given cutoff Λ , so we name the potential with each Λ "OBEPA". The parameters within the OBEPAs were fitted to NN scattering phase shifts, low-energy scattering data, and deuteron binding energy. Notably, for $\Lambda \leq 3 \text{ fm}^{-1}$, the potential matrix elements of our OBEPAs exhibit quantitative agreement with other realistic NN potentials evolved using the renormalization group (RG) method.

Both NR-BHF and RBHF calculations were conducted using these OBEPAs. The equations of state obtained

from BHF calculations at all cutoffs display an overbound nature. Notably, for $\Lambda \leq 3 \text{ fm}^{-1}$, the corresponding OBEPA demonstrate softness that prevents the production of saturation phenomena, aligning with prior studies emphasizing the significance of the three-nucleon force (3NF) in achieving nuclear matter saturation. Conversely, all EOSs derived from RBHF calculations exhibit saturation behaviors; however, their saturation densities and binding energies slightly fall short of accurately reproducing empirical saturation properties. Further investigations will explore the contributions arising from the relativistic three-hole-line component in the BBG expansion and the impact of genuine relativistic 3NFs.

We examined the relativistic saturation mechanism by analyzing the kinetic and potential terms within rel-

ativistic definitions. As the Dirac mass impacts the lower component of the spinor, high-density relativistic kinetic terms exhibit negativity, while significant repulsion arises in the potential terms due to the interplay between the attractive scalar self-energy and the repulsive time-component vector self-energy. Remarkably, even exceedingly soft potentials can generate substantial scalar and time-component vector self-energies, reaching several hundreds of MeV. The suppression of the attractive scalar self-energy and the linear growth of the repulsive time-component vector self-energy collectively contribute to the stiffening of the relativistic EOS without the incorporation of 3NFs. This scenario could lead to divergent interpretations of nuclear matter saturation and related phenomena.

-
- [1] K. Erkelenz, Current status of the relativistic two-nucleon one boson exchange potential, *Phys. Rep.* **13**, 191 (1974).
- [2] R. Machleidt, K. Holinde, and C. Elster, The bonn meson-exchange model for the nucleon-nucleon interaction, *Physics Reports* **149**, 1 (1987).
- [3] R. Machleidt, The meson theory of nuclear forces and nuclear structure, in *Adv. Nucl. Phys.*, Vol. 19, edited by e. a. J. W. Negele (Springer, USA, 1989) pp. 189–376.
- [4] R. Brockmann and R. Machleidt, Relativistic nuclear structure. i. nuclear matter, *Phys. Rev. C* **42**, 1965 (1990).
- [5] R. Machleidt, High-precision, charge-dependent bonn nucleon-nucleon potential, *Physical Review C* **63**, 024001 (2001).
- [6] T. Gross-Boelting, C. Fuchs, and A. Faessler, Covariant representation of the relativistic brueckner t-matrix and nuclear matter problem, *Nuclear Physics A* **648**, 105 (1999).
- [7] C. C. Wang, J. N. Hu, Y. Zhang, and H. Shen, The charge-dependent bonn potentials with pseudovector pion-nucleon coupling, *Chin. Phys. C* **43**, 114107 (2020).
- [8] C. C. Wang, J. N. Hu, Y. Zhang, and H. Shen, Properties of nuclear matter in relativistic brueckner–hartree–fock model with high-precision charge-dependent potentials, *J. Phys. G* **47**, 105108 (2020).
- [9] E. Epelbaum, W. Glöckle, and U.-G. Meißner, Low-momentum effective theory for nucleons, *Phys. Lett. B* **439**, 1 (1998).
- [10] E. Epelbaum, W. Glöckle, A. Krüger, and U.-G. Meißner, Effective theory for the two-nucleon system, *Nucl. Phys. A* **645**, 413 (1999).
- [11] E. Epelbaum, H.-W. Hammer, and U.-G. Meißner, Modern theory of nuclear forces, *Rev. Mod. Phys.* **81**, 1773 (2009).
- [12] S. K. Bogner, R. J. Furnstahl, and A. Schwenk, From low-momentum interactions to nuclear structure, *Prog. Part. Nucl. Phys.* **65**, 94 (2010).
- [13] R. Machleidt and D. R. Entem, Chiral effective field theory and nuclear forces, *Phys. Rep.* **503**, 1 (2011).
- [14] E. Epelbaum, W. Glöckle, and U.-G. Meißner, The two-nucleon system at next-to-next-to-next-to-leading order, *Nucl. Phys. A* **747**, 362 (2005).
- [15] K. Hebeler, S. K. Bogner, R. J. Furnstahl, A. Nogga, and A. Schwenk, Improved nuclear matter calculations from chiral low-momentum interactions, *Phys. Rev. C* **83**, 031301 (2011).
- [16] E. Epelbaum, Few-nucleon forces and systems in chiral effective field theory, *Prog. Part. Nucl. Phys.* **57**, 654 (2006).
- [17] S. K. Bogner, R. J. Furnstahl, and R. J. Perry, Three-body forces produced by a similarity renormalization group transformation in a simple model, *Ann. Phys.* **323**, 1478 (2008).
- [18] K. Hebeler, Three-nucleon forces: Implementation and applications to atomic nuclei and dense matter, *Phys. Rep.* **890**, 1 (2021).
- [19] A. Nogga, S. K. Bogner, and A. Schwenk, Low-momentum interaction in few-nucleon systems, *Phys. Rev. C* **70**, 061002 (2004).
- [20] S. K. Bogner, R. J. Furnstahl, P. Maris, R. J. Perry, A. Schwenk, and J. P. Vary, Convergence in the no-core shell model with low-momentum two-nucleon interactions, *Nucl. Phys. A* **801**, 21 (2008).
- [21] I. Tews, T. Krüger, K. Hebeler, and A. Schwenk, Neutron matter at next-to-next-to-next-to-leading order in chiral effective field theory, *Phys. Rev. Lett.* **110**, 032504 (2013).
- [22] C. Drischler, K. Hebeler, and A. Schwenk, Asymmetric nuclear matter based on chiral two- and three-nucleon interactions, *Phys. Rev. C* **93**, 054314 (2016).
- [23] C. Drischler, K. Hebeler, and A. Schwenk, Chiral interactions up to next-to-next-to-next-to-leading order and nuclear saturation, *Phys. Rev. Lett.* **122**, 042501 (2019).
- [24] J. Simonis, S. R. Stroberg, K. Hebeler, J. D. Holt, and A. Schwenk, Saturation with chiral interactions and consequences for finite nuclei, *Phys. Rev. C* **96**, 014303 (2017).
- [25] A. Ekström, G. Hagen, T. D. Morris, T. Papenbrock, and P. D. Schwartz, Δ isobars and nuclear saturation, *Phys. Rev. C* **97**, 024332 (2018).
- [26] J. Hoppe, C. Drischler, K. Hebeler, A. Schwenk, and J. Simonis, Probing chiral interactions up to next-to-next-to-next-to-leading order in medium-mass nuclei, *Phys. Rev. C* **100**, 024318 (2019).
- [27] F. Sammarruca and R. Millerson, Exploring the

- relationship between nuclear matter and finite nuclei with chiral two- and three-nucleon forces, *Phys. Rev. C* **102**, 034313 (2020).
- [28] J. M. Lattimer, The nuclear equation of state and neutron star masses, *Annu. Rev. Nucl. Part. Sci.* **62**, 485 (2012).
- [29] M. Oertel, M. Hempel, T. Klähn, and S. Typel, Equations of state for supernovae and compact stars, *Rev. Mod. Phys.* **89**, 015007 (2017).
- [30] T. Carreau, F. Gulminelli, and J. Margueron, General predictions for the neutron star crustal moment of inertia, *Phys. Rev. C* **100**, 055803 (2019).
- [31] C. C. Wang, J. Hu, Y. Zhang, and H. Shen, Properties of neutron stars described by a relativistic ab initio model, *Astrophys. J.* **897**, 96 (2020).
- [32] P. Danielewicz, R. Lacey, and W. G. Lynch, Determination of the equation of state of dense matter, *Sci* **298**, 1592 (2002).
- [33] A. Le Fèvre, Y. Leifels, W. Reisdorf, J. Aichelin, and C. Hartnack, Constraining the nuclear matter equation of state around twice saturation density, *Nucl. Phys. A* **945**, 112 (2016).
- [34] H. Wolter *et al.* (TMEP), Transport model comparison studies of intermediate-energy heavy-ion collisions, *Prog. Part. Nucl. Phys.* **125**, 103962 (2022).
- [35] B. D. Day, Current state of nuclear matter calculations, *Rev. Mod. Phys.* **50**, 495 (1978).
- [36] V. R. Pandharipande and R. B. Wiringa, Variations on a theme of nuclear matter, *Rev. Mod. Phys.* **51**, 821 (1979).
- [37] J. W. Clark, Variational theory of nuclear matter, *Prog. Part. Nucl. Phys.* **2**, 89 (1979).
- [38] B. D. Day, Brueckner-bethe calculations of nuclear matter, *Nucl. Phys. A* **328**, 1 (1979).
- [39] M. Hjorth-Jensen, T. T. S. Kuo, and E. Osnes, Realistic effective interactions for nuclear systems, *Phys. Rep.* **261**, 125 (1995).
- [40] F. Coester, S. Cohen, B. Day, and C. M. Vincent, Variation in nuclear-matter binding energies with phase-shift-equivalent two-body potentials, *Phys. Rev. C* **1**, 769 (1970).
- [41] B. D. Day and F. Coester, Influence of virtual Δ states on the saturation properties of nuclear matter, *Phys. Rev. C* **13**, 1720 (1976).
- [42] B. D. Day, Nuclear saturation from two-nucleon potentials, *Phys. Rev. Lett.* **47**, 226 (1981).
- [43] Z. H. Li, U. Lombardo, H.-J. Schulze, W. Zuo, L. W. Chen, and H. R. Ma, Nuclear matter saturation point and symmetry energy with modern nucleon-nucleon potentials, *Phys. Rev. C* **74**, 047304 (2006).
- [44] S. K. Bogner, A. Schwenk, R. J. Furnstahl, and A. Nogga, Is nuclear matter perturbative with low-momentum interactions?, *Nucl. Phys. A* **763**, 59 (2005).
- [45] C. J. Horowitz and B. D. Serot, The relativistic two-nucleon problem in nuclear matter, *Nuclear Physics A* **464**, 613 (1987).
- [46] L. Sehn, C. Fuchs, and A. Faessler, Nucleon self-energy in the relativistic brueckner approach, *Phys. Rev. C* **56**, 216 (1997).
- [47] C. Fuchs, T. Waindzoeh, A. Faessler, and D. S. Kosov, Scalar and vector decomposition of the nucleon self-energy in the relativistic brueckner approach, *Phys. Rev. C* **58**, 2022 (1998).
- [48] P. Ring, Relativistic mean field theory in finite nuclei, *Progress in Particle and Nuclear Physics* **37**, 10.1016/0146-6410(96)00054-3 (1996).
- [49] S. H. Shen, J. N. Hu, H. Z. Liang, J. Meng, P. Ring, and S. Q. Zhang, Relativistic brueckner—hartree—fock theory for finite nuclei, *Chin. Phys. Lett.* **33**, 102103 (2016).
- [50] S. H. Shen, H. Z. Liang, J. Meng, P. Ring, and S. Q. Zhang, Fully self-consistent relativistic brueckner-hartree-fock theory for finite nuclei, *Phys. Rev. C* **96**, 014316 (2017).
- [51] S. B. Wang, Q. Zhao, P. Ring, and J. Meng, Nuclear matter in relativistic brueckner-hartree-fock theory with bonn potential in the full dirac space, *Phys. Rev. C* **103**, 054319 (2021).
- [52] S. B. Wang, H. Tong, and C. C. Wang, Nuclear matter within the continuous choice in the full dirac space, *Phys. Rev. C* **105**, 054309 (2022).
- [53] V. G. J. Stoks, R. A. M. Klomp, C. P. F. Terheggen, and J. J. de Swart, Construction of high-quality nn potential models, *Phys. Rev. C* **49**, 2950 (1994).
- [54] O. Dumbrajs, R. Koch, H. Pilkuhn, G. C. Oades, H. Behrens, J. J. de Swart, and P. Kroll, Compilation of coupling constants and low-energy parameters, *Nucl. Phys. B* **216**, 277 (1983).
- [55] W. H. Long, N. V. Giai, and J. Meng, Density-dependent relativistic hartree-fock approach, *Phys. Lett. B* **640**, 150 (2006).
- [56] W. H. Long, H. Sagawa, N. V. Giai, and J. Meng, Shell structure and ρ -tensor correlations in density dependent relativistic hartree-fock theory, *Phys. Rev. C* **76**, 034314 (2007).
- [57] S. K. Bogner, R. J. Furnstahl, S. Ramanan, and A. Schwenk, Low-momentum interactions with smooth cutoffs, *Nucl. Phys. A* **784**, 79 (2007).
- [58] R. B. Wiringa, V. G. J. Stoks, and R. Schiavilla, Accurate nucleon-nucleon potential with charge-independence breaking, *Phys. Rev. C* **51**, 38 (1995).
- [59] D. R. Entem, R. Machleidt, and Y. Nosyk, High-quality two-nucleon potentials up to fifth order of the chiral expansion, *Phys. Rev. C* **96**, 024004 (2017).
- [60] G. E. Brown, A. D. Jackson, and T. T. S. Kuo, Nucleon-nucleon potential and minimal relativity, *Nucl. Phys. A* **133**, 481 (1969).
- [61] M. Baldo, I. Bombaci, L. S. Ferreira, G. Giansiracusa, and U. Lombardo, Nuclear matter within the continuous choice, *Phys. Rev. C* **43**, 2605 (1991).